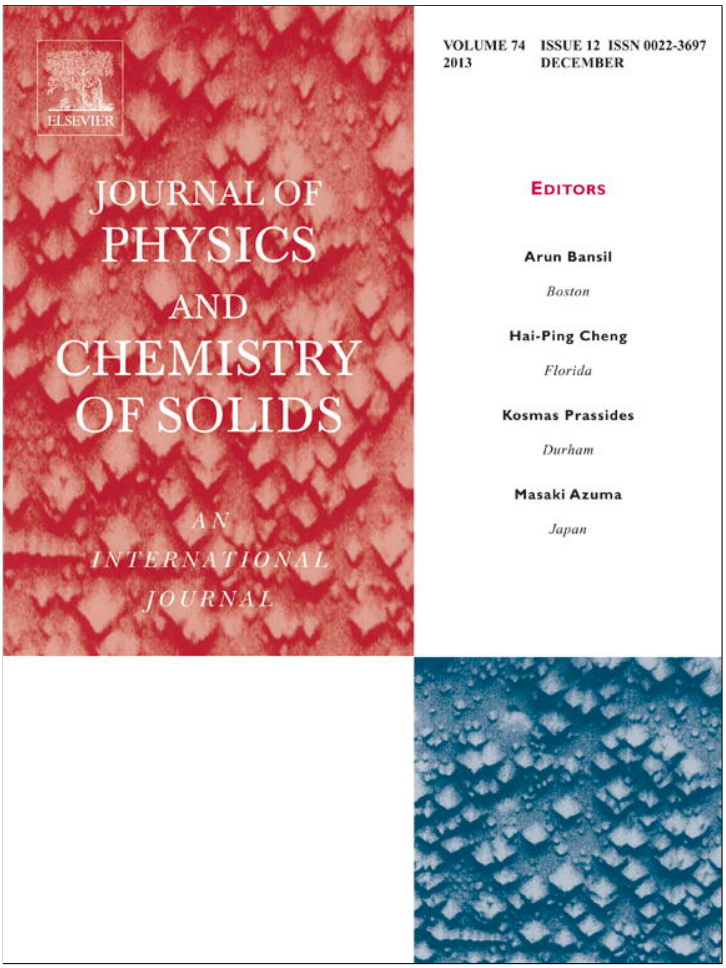

Journal of Physics and Chemistry of Solids 74 (2013) 1695–1702

Contents lists available at ScienceDirect

Journal of Physics and Chemistry of Solids

journal homepage: www.elsevier.com/locate/jpcs

Dielectric behavior, conduction and EPR active centres in $BiVO_4$ nanoparticles

Rajalingam Venkatesan [a,b], Subramaniam Velumani [a,c], Mohamed Tabellout [b], Nicolas Errien [b], Abdelhadi Kassiba [b,*]

[a] Nanoscience and Nanotechnology Program, CINVESTAV-IPN, Zacatenco, Av IPN #2508, Col Zacatenco, D.F., C.P. 07360, Mexico
[b] Institute of Molecules and Materials of Le Mans (I3M), UMR-CNRS 6283, Faculté des Sciences et Techniques Université du Maine, 72085 Le Mans Cedex 9, France
[c] Department of Electrical Engineering (SEES), CINVESTAV-IPN, Zacatenco, Av IPN #2508, Col Zacatenco, D.F., C.P. 07360, Mexico

ARTICLE INFO

Article history:
Received 17 October 2012
Received in revised form
20 June 2013
Accepted 25 June 2013
Available online 10 July 2013

Keywords:
Nanostructures
Oxides
Dielectric properties
Electron paramagnetic resonance (EPR)

ABSTRACT

Bismuth vanadate ($BiVO_4$) nanomaterials were synthesized by mechano-chemical ball milling method and complementary investigations were devoted to their structures, nanoparticle morphologies and electronic active centres. The dielectric and conductivity behaviour were analysed systematically in wide temperature and frequency ranges to correlate such physical responses with the peculiarities of the samples. Large interfacial polarisations favoured by high specific surfaces of nanoparticles account for a drastic enhancement of the dielectric function in the quasi-static regime. Exhaustive analyses of the dielectric experiments were achieved and account for the main features of dielectric functions and their related relaxation mechanisms. The electrical conductivity is thermally activated with energies in the range 0.1–0.6 eV depending on the sample features. DC conductivity up to 10^{-3} S/cm was obtained in well crystallized nanoparticles. Vanadium ions reduction was revealed by EPR spectroscopy with higher concentrations of the active centres (V^{4+}) in more agglomerated and amorphous nanopowders. The EPR spectral parameters of V^{4+} were determined and correlated with the local environments of reduced vanadium ions and the characteristics of their electronic configurations. An insight is also made on the role of active electronic centres (V^{4+}) on the conduction mechanism in nanostructured $BiVO_4$.

1. Introduction

Nanostructured materials offer the possibility to modulate in large extent their physical features including mechanical, electronic, optical and magnetic, compared to their parent bulk state. Due to the advantages from the nanostructuration of functional materials, we have considered the case Bismuth Vanadate ($BiVO_4$) which is worthwhile with regard to their ferroelastic [1,2] and photocatalytic properties [3,4]. This class of materials possesses three main crystalline forms such as tetragonal zircon, monoclinic scheelite and tetragonal scheelite structures [5]. For some applications, thin films of $BiVO_4$ have been used as photo-anodes with high quantum efficiency in water decomposition [6]. On the other hand, for samples as nanoparticles, high specific surfaces, controlled chemical composition and crystalline order are important features for their subsequent applications [7]. However, main drawbacks of nanostructured systems lie in the active electronic centres and reconstruction of the outermost nanoparticle surfaces [8]. For $BiVO_4$, mixed valence of vanadium ions is expected to occur with a large concentration due to the high specific surfaces. These effects alter drastically the electronic and optical behavior of the systems as well as their reactivity for catalytic applications.

The ambition of the work is to contribute for the first time to a systematic study on $BiVO_4$ nanostructures obtained with different milling conditions. With respect to these physical features, there are no related reports available on nanostructured $BiVO_4$ even though we can see some investigations of $Bi_4V_2O_{11-z}$, $Bi_2VO_{5.5}$ [9,10] etc. Dielectric and conduction behaviors are mainly considered as well as the investigations by electron paramagnetic resonance (EPR) of the active electronic centers which can alter significantly the concentration of charge carriers and their mobility. These investigations were performed without any doping by external elements. Thus, EPR signal in nanostructured $BiVO_4$ is associated to the valance states of reduced V^{4+} which may result from the stoechiometry of the sample such as oxygen deficiencies or from the surface states. EPR investigations clarify the surface or bulk location of V^{4+} in the structures and their local environments. This information may be used to show the role of paramagnetic centres on the photocatalytic activity without using additional doping agents as for example the case of molybdenum doped

* Corresponding author. Tel.: +33 2 43 83 35 12; fax: +33 2 43 83 35 18.
E-mail address: kassiba@univ-lemans.fr (A. Kassiba).

0022-3697/$ - see front matter © 2013 Elsevier Ltd. All rights reserved.
http://dx.doi.org/10.1016/j.jpcs.2013.06.011

$BiVO_4$ [11]. No such doping effects will be considered in this report and we limit to intrinsic occurrence of paramagnetic ions induced at the surfaces of low dimension particles or favored by oxygen vacancies [12].

The dielectric behavior can be used to monitor the role of interfaces in nanostructures. The main effect is related to interfacial polarizations with enhanced strength due to large specific surfaces [13]. The physical responses such as the dielectric functions with their real and imaginary part [ε' (ω), ε'' (ω)] were measured in wide temperature and frequency ranges. The real part ε' (ω) yields information on the polarization effects while the imaginary part ε'' (ω) accounts for the losses induced notably by conduction processes. Analyses of the experiments by relevant models yields the quasi-static dielectric constant and dc conductivity as well as their characteristic relaxations times. Conduction phenomena and dielectric relaxations were quantitatively interpreted taking into account the microstructure and crystalline order of the nanoparticles. Correlations between the conductivity and the active electronic centers probed by EPR were also discussed.

2. Experimental details and procedures

2.1. Mechano-chemical synthesis

Mechano-chemical syntheses were carried out in a planetary ball mill (Retsch, planetary ball mill PM 400). The chemicals reactants Bi_2O_3 (99.999%) V_2O_5 (99.99%) were purchased from Sigma Aldrich and used without further purification. Starting powders were initially homogenized by hand mixing in an agate mortar and placed in a tungsten carbide vial (80 ml) with tungsten carbide balls (10 mm as diameter). The operating ball milling speed was fixed at 400 rpm but different ball-to-powder ratios (BPR) and milling times were adopted. BPR about 5:1 (5 balls used with a fixed amount of powder) was mainly used with milling times about 11, 16 and 24 h. Other synthesis conditions were adopted such as BPR about 8:1 or 10:1 and a time duration about 11 h. Even though the synthesis conditions were varied in a wide extent right from the time of 11 h to 24 h and BPR from 5:1 to 10:1, we report here only the investigations on key representative samples; i.e. A (11 h 10:1) and B (24 h 5:1).

Structural analysis was performed by PANalytical X-ray diffractometer with Cu$K\alpha$ ($\lambda = 1.5406$ Å) radiation. The FESEM analysis was performed by Carl Zeiss Auriga 60, nanotechnology system.

2.2. Dielectric experiments

Dielectric relaxation spectroscopy (DRS) measurements were performed over a wide frequency range (0.1 Hz to 10 MHz) using Novocontrol Broadband Dielectric Spectrometer. To cover the experiments in a wide frequency domain, a Solartron S l1260 combined with a broadband dielectric converter (BDC) were used to obtain impedance measurements. The method is well adapted for classes of materials with a low conductivity ($\leq$1 S/cm) or insulating materials. Fine and homogenous powders of $BiVO_4$ were compacted into cylindrical pellets of 5 mm diameter and 1 mm thickness by applying a uniaxial pressure of 17 MPa with a hydraulic pressure. The contact between the electrodes and the sample is enough good that we do not need any improvement through metal deposition on the surfaces. The low frequency dispersion shown on all our curves is no longer connected with sample-electrode contact but with the existence of ionic charges which polarize the electrodes. In the fitting procedure of dielectric function we haven't taken into account the experimental low frequency values. Then, the determined parameters are sound and account correctly for the intrinsic dielectric behaviour of samples. On the other hand, the reproducibility of the measurements makes us confident in the non-relevant contribution connected with some kind of porosity. Such approach was applied in several former works on other kind of nanopowders such as SiC nanomaterials [13,14].

The experimental setup consists in the sample as a pellet placed between two golden plate electrodes to form a capacitor. The sample temperature was varied between 173 K and 533 K by using a gas stream of nitrogen with a controlled temperature close to the sample within the accuracy of $\pm$0.1 K.

2.3. EPR investigations

EPR experiments were performed on EMX-Bruker spectrometer working in the X-Band (9.5 GHz). The EPR signal is related to Vanadium ions (V^{4+}) which occur in the samples due to the stoechiometry departure as oxygen vacancies in $BiVO_4$ structures or from nanoparticle surfaces. The measurements were made at different temperatures by using Oxford cryostat in the range (4–300 K). The resonance positions of the EPR lines were accurately evaluated by using a characteristic EPR line of dry DPPH sample associated to g-factor about 2.0036. Experimental parameters such as the microwave power, the modulation field and the detection frequency were chosen to avoid any EPR line shape distortion. Also, a typical modulation field about 1–5 Gauss and frequency modulation about 100 kHz were used. The recorded EPR spectra were adjusted by using Bruker commercial software Winsinfonia. These simulations give the magnetic g-tensor components as well as the hyperfine parameters related to the nuclear spin of Vanadium ions.

3. Experimental results and discussions

3.1. Structural and morphology studies

The crystalline structure and purity of as-prepared samples were investigated by XRD as illustrated in Fig. 1 for A and B samples. The refinement of the XRD patterns by FULLPROF

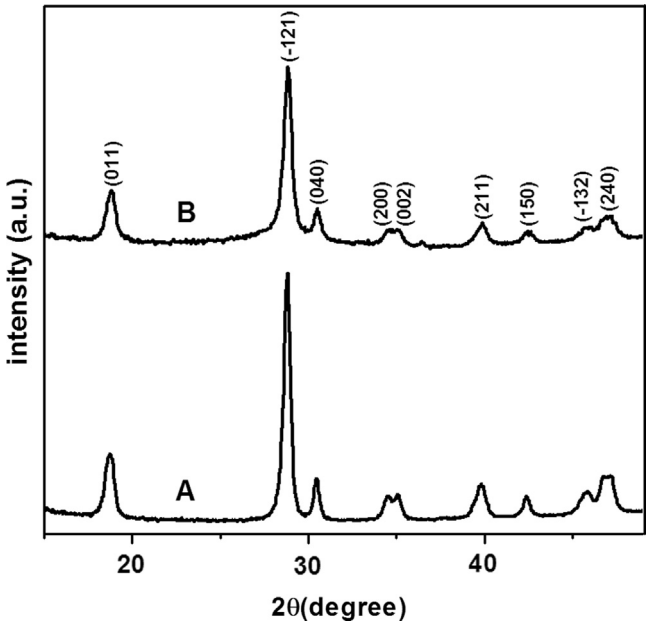

Fig. 1. XRD patterns of the monoclinic $BiVO_4$ samples A and B obtained by high energy ball milling process.

software assign the structures to a pure monoclinic scheelite phase with lattice constants $a=5.200$ Å, $b=11.710$ Å and $c=5.140$ Å. This is in agreement with the reported values of $a=5.1950$ Å, $b=11.701$ Å and $c=5.092$ Å (JCPDS no. 14-0688). Additionally, based on the FWHM, we can clearly see in Fig. 1 that sample A shows better crystalline order compared to sample B. It is worth noting that whatever the synthesis conditions, XRD results confirm that a single crystallized monoclinic $BiVO_4$ phase was obtained. The only difference concerns the improved crystalline order by using low milling time (11 h).

The FESEM microstructural investigations reveal the features of the surface morphology for samples A and B (Fig. 2). In general, once powders are ball milled, cold welding becomes the predominant process resulting in the agglomeration of the particles with increasing ball-milling time [15]. This is the case of B sample which is composed by clusters made from agglomerated and welded particles while the A sample, obtained by short milling time, exhibits individual small nanoparticles with sizes in the order of 20 nm.

3.2. Dielectric investigation

3.2.1. Theoretical background

The frequency dependence of complex dielectric function $\varepsilon^*(\omega)$ is accounted correctly by using the generalized Havriliak–Negami (HN) model [16]:

$$\varepsilon^*(\omega)=\varepsilon'(\omega)-i\varepsilon''(\omega)=\frac{\sigma_{dc}}{i\varepsilon_0\omega}+\varepsilon_\infty+\frac{\Delta\varepsilon}{(1+(i\omega\tau)^\alpha)^\beta} \quad (1)$$

In this expression, dielectric strength $\Delta\varepsilon$ represents the difference between the quasi-static dielectric permittivity ε_s and the high frequency one referred as ε_∞. The coefficient τ corresponds to a characteristic time related to the dielectric relaxation phenomena which are also closely related to the conductivity process as will be discussed below. The phenomenological parameters α and β, in the range $0<\alpha, \beta<1$, are related to the distribution of relaxation times due to some inhomogeneous processes which may be induced by nanocrystallite sizes or surface effects on $BiVO_4$ nanoparticles. In the simple case of Arrhenius process, the dielectric relaxation is characterized by a unique relaxation time τ_0 leading to $\alpha=1$ and $\beta=1$. For a general case, we may only give asymptotic behavior of $\varepsilon''(\omega)$ in the low and high frequency range with respect to the characteristic relaxation times. The tendencies are expressed in term of α and β such as $\varepsilon''\propto\omega^\alpha$ when $\omega\tau\ll1$ and $\varepsilon''\propto\omega^{-\alpha\beta}$ for $\omega\tau\gg1$. From the plot of dielectric functions, the parameter τ is closely related to the value of the frequency where the maximum of dielectric loss peak is located. The coefficients α and β can be estimated only by an adjustment of experimental curves according to Eq. (1). For the frequency dependent (ac) and steady state (dc) conductivities, they are determined from the relation between the complex conductivity and dielectric function; i.e. $\sigma^*(\omega)=i\omega\times\varepsilon_0\varepsilon^*(\omega)$.

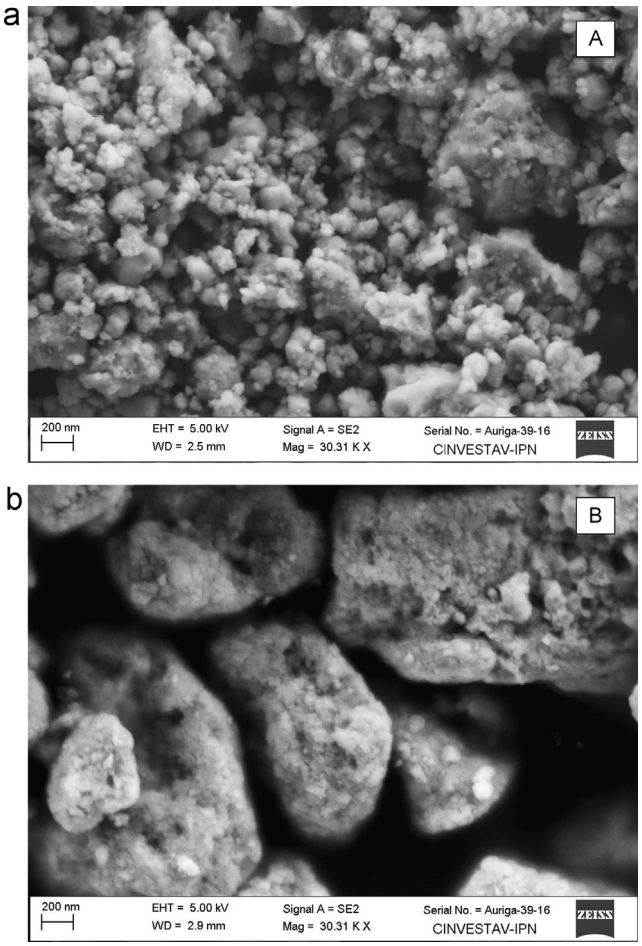

Fig. 2. FESEM micrographs of the samples A and B which show the different microstructures and morphologies of the representative samples A and B.

3.2.2. Dielectric measurements and analysis

Fig. 3 summarizes the experimental results for real (Fig. 3(a) and (c)) and imaginary (Fig. 3(b) and (d)) parts of the dielectric functions related to A and B samples. The frequency dependence of the dielectric function $\varepsilon'(\omega)$ reflects dynamic processes with thermally dependant relaxation phenomena. The dielectric behavior at low frequencies (LF) which manifests through the divergence of $\varepsilon'(\omega)$ is related to electrodes polarization induced by ionic conductivity being thermally activated with raising the temperature. Excluding this LF divergent contribution, the adjustment of dielectric data is well accounted by Havriliak–Negami model depicted as continuous lines in Fig. 3. In this simulation, the same set of fitting parameters was used for both real and imaginary parts of dielectric function as well as for the frequency dependant conductivity. This procedure allows obtaining sound values and makes us confident in the parameters evaluated by this model. The calculated asymptotic behavior of ε' in the quasi-static regime is assigned to the dielectric constant which is indicative of large interfacial polarizations. Indeed, the quasi-static values of ε' are about 140 and 170, respectively, for the samples A and B which represent twice the value 68 reported for the bulk $BiVO_4$ [17]. This is consistent with the large specific surfaces of nanoparticles where interfacial polarizations enhance the asymptotic dielectric constants in the quasi-static regime [13]. In order to support the relevance of interfacial polarizations invoked above, the Nyquist plot for the sample B at temperature about 273 K is shown in Fig. 4. Qualitatively, three main frequency variation regimes can be distinguished in the plot. The high frequency (HF) side is related to intrinsic behaviour involved in the nanoparticles core. The intermediate region (IF) corresponds to the intra-particles contribution related to interfacial polarizations. The third part shown in the low frequency regime (LF) is plausibly induced by the electrode polarizations leading to the LF dispersion. Exhaustive modelling of the Nyquist diagrams of heterogeneous systems (core, interfaces) requires suitable models as a set of RC cells [18] or constant phase elements (CPE) [19]. This will be reported in separate contribution.

Finally, the imaginary dielectric functions ε'' versus ω were correctly adjusted by using HN model and the results summarized in Fig. 3(b) and (d). Following the frequency range, different

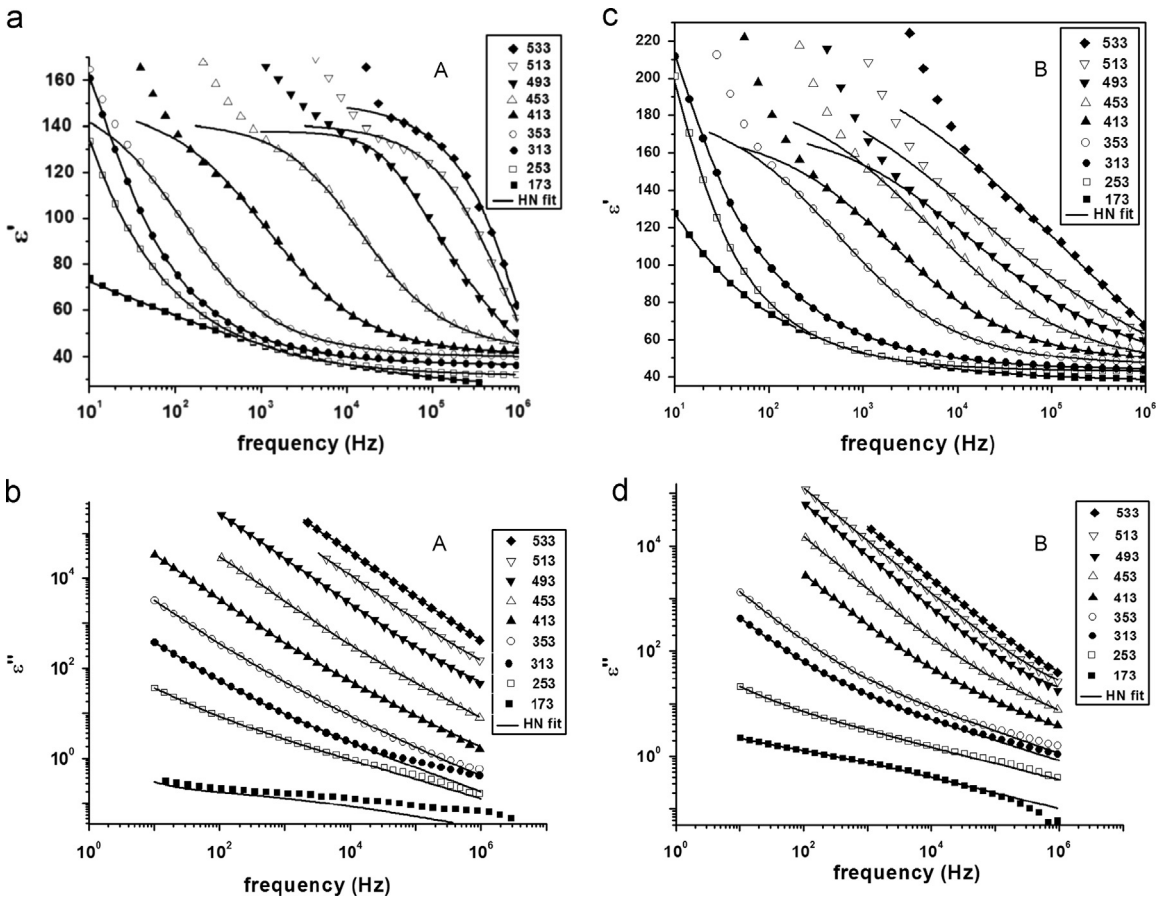

Fig. 3. Temperature and frequency dependencies of real and imaginary dielectric permittivity in $BiVO_4$ nanopowders of sample A ((a) and (b)) and sample B ((c) and (d)), continuous lines are fits obtained by Havriliak–Negami model.

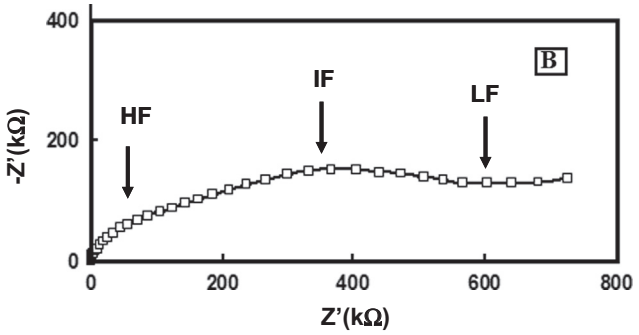

Fig. 4. Nyquist plot of the imaginary part of the impedance versus its real part for the sample B at temperature about 273 K. Indications are also given on the frequency range HF, IF and LF designating, respectively, high, intermediate and low frequency regimes.

variation regimes of $\varepsilon''(\omega)$ are involved. Thus, the linear variation accounted by the first term of Eq. (1) indicates that steady state dc conductivity exists and increases with the temperature. The low frequency side of $\varepsilon''(\omega)$ is then dominated by the dc conductivity contribution while the higher frequencies asymptotic behavior is given by $\varepsilon''(\omega) \propto \omega^{-\alpha\beta}$ with $\alpha\beta$ in the range 0.8–0.9.

3.2.3. *Frequency and temperature dependent conductivity*

The electrical conductivities of the as-prepared samples A and B were determined from the dielectric measurements and reported in Fig. 5. The conductivity curves display similar features for the two $BiVO_4$ samples. The asymptotic values at low frequency ($\omega \to 0$) correspond to the dc conductivities σ_{dc} summarized in function versus the temperature in Fig. 6. The obtained values depend on the milling times and also on the temperature through thermally activated conduction process. The semi-log plot of σ_{dc} versus the inverse of temperature $(1000/T)$ follows an Arrhenius activated law as

$$\sigma_{dc}^{i}(T) = \sigma_0^i \times \exp\left(-\frac{E_a^i}{kT}\right)$$

where σ_0^i is pre-exponential factor and k is the Boltzmann constant. However, two regimes are involved with different activation energies (E_a^i). The cross-over temperature between regimes is found relatively close to $T_c = 300$ K with a net difference between the samples A and B through the cusp-shape of the conductivity evolution around T_c. Indeed, more rounded and defined curve shape is observed for A sample (11 h milling time) while an abrupt change of the curve slope is noticed for B sample (24 h milling time). The activation energies about 0.621 eV and 0.242 eV for A and B samples, respectively, in the temperature range 373–533 K change to 0.142 eV and 0.123 eV in the temperature range 173–293 K. Low activation energies are required for longer milling times and indicate low barrier heights on the conduction channels. These features can be correlated with the microstructure of the samples. Indeed, sample A is composed by smaller nanoparticles compared to sample B where larger particles were found. Also, the microstructure with low density of interfaces (large particles) requires only low activation energies for the

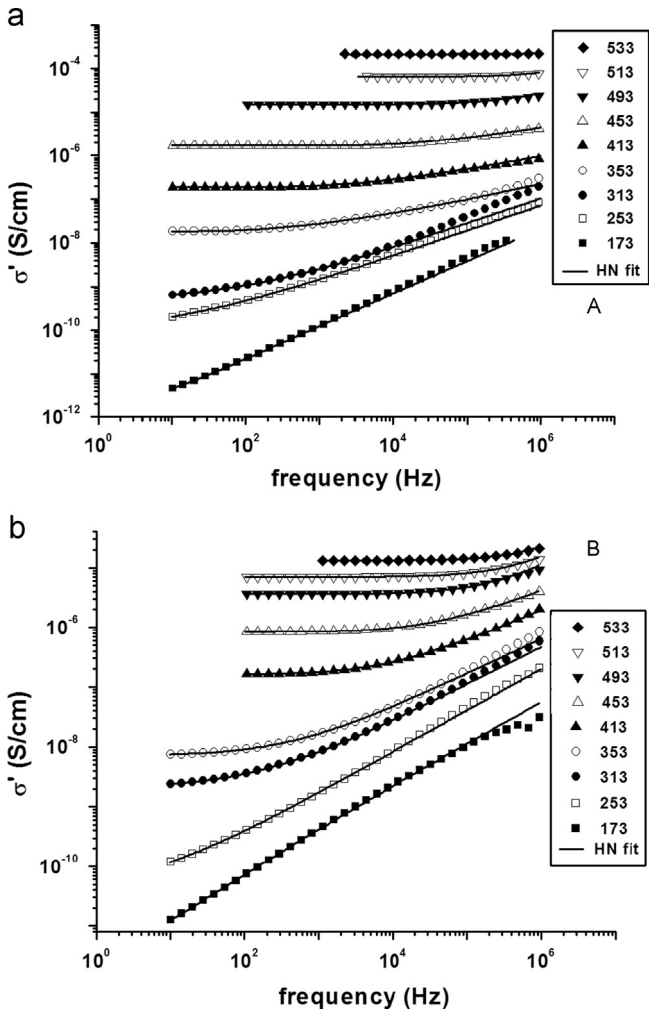

Fig. 5. Frequency dependent (ac) of real part of conductivity $\sigma'(\omega)$ for different temperatures: (a) A sample and (b) B sample. The continuous lines are fits by Havriliak–Negami model.

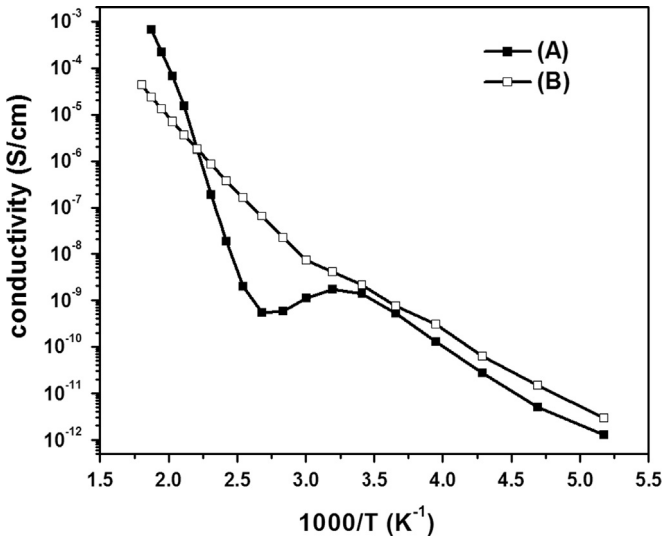

Fig. 6. Variation of the dc conductivity versus the inverse temperature for the samples A and B.

charge carriers. The EPR part discussed below will clarify additional aspects related to the charge carriers features in these systems.

3.2.4. Temperature dependence of relaxation times

The relaxation times characterize the dynamics of processes induced in the samples by dipolar relaxation or charge carriers mobility under alternative voltages. As shown from dielectric functions discussed above, the relaxation mechanisms are too complex to be analyzed or accounted by unique relaxation time as it can be involved in the simple Debye model [20]. A distribution of relaxation times (DRT) is more relevant and may be accounted for by the well-known Havriliak–Negami phenomenological model. In this case, the parameters (α,β) define the shape of the dielectric functions and inform on the occurrence of DRT. During the adjustment of the experiments by HN model, (α,β) were varied as function of temperature in the range [0.6–1.0] but no clear tendency is inferred. What can be addressed is only the relevance of DRT in the investigated samples. The relaxation time τ_{max} (Fig. 7) was determined by fitting the dielectric function curves $\varepsilon'(F)$ and $\varepsilon''(F)$. When we compare the obtained values with those deduced, when it is possible, from the frequency associated to the maximum of $\varepsilon''(F)$; namely $1/2\pi\tau_{max}$, the agreement is quite good. In the case when the maximum is not clearly defined or outside the range of frequency, only the evaluated value by fitting is reported as τ_{max}.

For both samples, the average relaxation time is nearly stationary at low temperatures. However, rising the temperature leads to an abrupt decrease around 350 K for the sample A while lower crossover temperature about 310 K was obtained for sample B. Such behavior is intimately correlated with the thermal evolution of the dc conductivities (Fig. 6) which show changes in the activation energies of charge carriers. An additional argument supporting the intimate link between σ_{dc} and τ_{max} is illustrated in Fig. 8 where these parameters are proportional to each other in the considered temperature range. This behavior was also demonstrated in nanostructured materials and a tentative explanation underlines the influence of the thermally activated charge motions on dielectric relaxation characteristic times [12].

To sum up, the thermally activated conductivity of two representative nanostructured $BiVO_4$ samples is in the order of 10^{-3}–10^{-4} S/cm at $T=533$ K. Two main thermal evolution regimes were demonstrated with a crossover at critical temperature about 310 K. The activation energies depend on the considered temperature ranges, on the microstructure and crystalline order of the samples which modulate the height of barriers acting on the conduction channels.

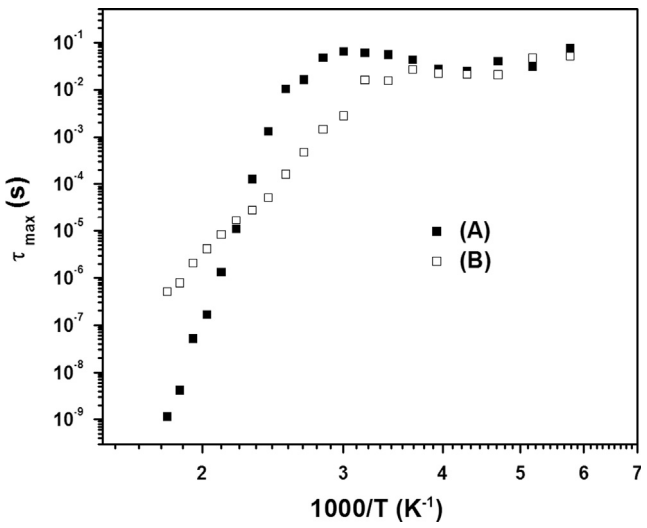

Fig. 7. Temperature dependence of relaxation time in $BiVO_4$ obtained under different synthesis conditions of samples A and B.

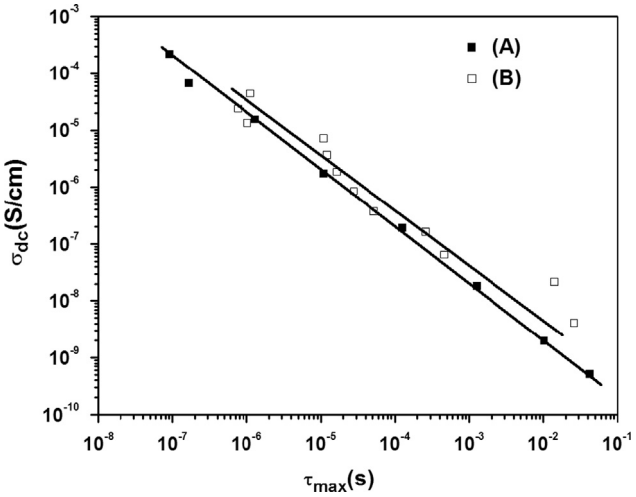

Fig. 8. Log–log plot of the d.c conductivity versus the relaxation time for the samples A and B.

3.3. EPR investigations

3.3.1. Theoretical background

Without impurities or any doping ions in the chemical reactants used for $BiVO_4$ synthesis, the EPR signal may be induced by a reduction of Vanadium ions. Indeed, in a perfect crystalline structure, vanadium ions have valence state V^{5+} and then no EPR signal may be observed. If oxygen vacancies occur due to organisation or morphologies of the samples as nanoparticles with high specific surfaces, some vanadium ions can be reduced to V^{4+}. This is favoured by the possibility for V^{4+} to adopt octahedral as well as pyramidal oxygen environments which may occurs at the outermost particle surfaces or when vacancies are involved in the bulk. The resulting electronic configuration of reduced vanadium ions, V^{4+} ($3d^1$), possesses an effective electronic spin ($S=1/2$) giving rise to an EPR signal. In addition, the vanadium nuclei with the main isotope ^{51}V(99.5%) is characterized by nuclear spin ($I=7/2$) which gives rise to quite characteristic substructures on the EPR spectrum (hyperfine splitting). From a theoretical basis, the interactions on vanadium ions consist mainly in coupling between electronic spin and external magnetic field (Zeeman interaction) and also the coupling between electronic and nuclear spin (hyperfine interaction). The interactions define the spin Hamiltonian as follows:

$$\hat{H} = \beta(B_x g_x \hat{S}_x + B_y g_y \hat{S}_y + B_z g_z \hat{S}_z) + (A_x \hat{S}_x \hat{I}_x + A_y \hat{S}_y \hat{I}_y + A_z \hat{S}_z \hat{I}_z)$$

In this expression, β represents the Bohr magneton and the frame (x,y,z) refers to the principal axes of g-tensor with the components $g_{x,y,z}$. The components $B_{x,y,z}$ are related to the applied static magnetic field and $A_{x,y,z}$ represent the hyperfine tensor (A-tensor) parameters which characterize the strength of the hyperfine coupling [21].

The experimental EPR spectra are adjusted by using Bruker–Winsinfonia software and considering the interactions summarized above. The procedure of fitting determines the magnetic fields (B_{ir}) related to all transitions between spin states (both electronic and nuclear states are considered as well). By using derivative of lorentzian lines centred at the different B_{ir} and suitable line-width, we can reproduce precisely all the features of the experimental spectra. This allows extracting the g_X, g_Y, g_Z components and the hyperfine coupling parameters summarized in Table 1.

The spectral parameters reflect the symmetry of local environments around paramagnetic ions as well as features of the electronic wave-functions and residence probabilities of unpaired electrons close to the nuclei [8,21]. Particularly, the g-tensor components exhibit departures ($\Delta g_{x,y,z}$) with respect to the Landé g-factor of free electron ($g=2.0023$). These shifts depend on the spin–orbit coupling and on the energies of the fundamental and excited orbitals occupied by unpaired electrons. The interpretation of the parameters underlines the main features of the environments of V^{4+} ions and their electronic peculiarities contributing then to better understanding of the conductivity features in this class of materials and also their relevance in catalysis processes.

Table 1
EPR spectral parameters of V^{4+} in $BiVO_4$ obtained by mechano-chemical synthesis with different milling times and BPR parameters exemplified by the samples A and B with the characteristics defined in the text.

Samples	*Ax*	*Ay*	*Az*	*Gx*	*gy*	*gz*	*ΔHx*	*ΔHy*	*ΔHz*
A	30	72	199	1.97	1.980	1.930	75	30	100
B	20	75	200	1.97	1.985	1.930	25	30	85

3.3.2. EPR spectral analysis

The EPR spectra recorded on the two representative samples (Fig. 9(a) and (b)) reveal anisotropy features on magnetic and hyperfine tensors leading to the different substructures. The simulation of the EPR spectra requires two main contributions depicted in Fig. 9(c). The first anisotropic signal is related to isolated V^{4+} ions with orthorhombic local symmetry. The second contribution consists in a single broad line (200 Gauss as line width) without any details such as hyperfine structure or resolved substructure. Vanadium pairs or clustering of V^{4+} ions can account for the broad background absorption line. In all samples, the anisotropic EPR spectrum is characterized by g-tensor consistent with orthorhombic local symmetry around V^{4+} with the components $g_x = 1.970$, $g_y = 1.980-1.985$, $g_z = 1.930-1.935$. This is understood by the occurrence of similar electronic structure and local environment of V^{4+} in $BiVO_4$ irrespective to the sample microstructures (A, B). From a theoretical approach, the electronic structure $3d^1$ of V^{4+} ions in tetrahedral environment consists in fundamental state $d_{x^2-y^2}$ with the energy $E_{x^2-y^2}$ and the excited states as d_{xy}, d_{xz}, d_{yz} with the energies ($E_{ij(xy,xz,yz}$). The components of the g-tensor can be expressed in terms of the spin–orbit coupling between the fundamental and excited states [22] as Eq. (2) below.

$$g_x = g_e - \frac{2\lambda_0 \chi^2_{x^2-y^2}\chi^2_{yz}}{(E_{x^2-y^2}-E_{yz})}$$
$$g_y = g_e - \frac{2\lambda_0 \chi^2_{x^2-y^2}\chi^2_{xz}}{(E_{x^2-y^2}-E_{xz})}$$
$$g_z = g_e - \frac{8\lambda_0 \chi^2_{x^2-y^2}\chi^2_{xy}}{(E_{x^2-y^2}-E_{xy})} \quad (2)$$

with $g_e=2.0023$ for a free electron, λ_0 is the spin–orbit coupling and χ^2_{ij} the fraction of d_{ij} anti-bonding orbitals of the Vanadium–oxygen complexes. Such Eq. (2) are used to understand even roughly the features of the electronic configuration related to V^{4+} ions. From the values of the g-tensor components we may notice that the local symmetry is nearly axial with $g_\perp \approx (g_x + g_y/2) \approx 1.978$ and $g_{//} = 1.933$. The splitting of the electronic diagram related to V^{4+} maybe then assigned to $\Delta_{//} = E_{x^2-y^2} - E_{xy} < \Delta_\perp \approx E_{x^2-y^2} - E_{yz} \approx E_{x^2-y^2} - E_{xz}$. By using the free vanadium ion spin–orbit coupling parameter $\lambda_0 \approx 240$ cm^{-1}, $\Delta_{//} = 12,500$ cm^{-1}, $\Delta_\perp = 14,400$cm^{-1}, and taking the fraction of fundamental orbital $d_{x^2-y^2}$ in the anti-bonding wave-function as $\chi^2_{x^2-y^2} = 1$, a rough estimation is then given for the contributions of the excited states $\chi^2_{xz} = \chi^2_{yz} = 0.6$ and $\chi^2_{xy} = 0.5$. These fractions of excited states in the wave-function of unpaired d-electron are quite high, hence are the optical transition

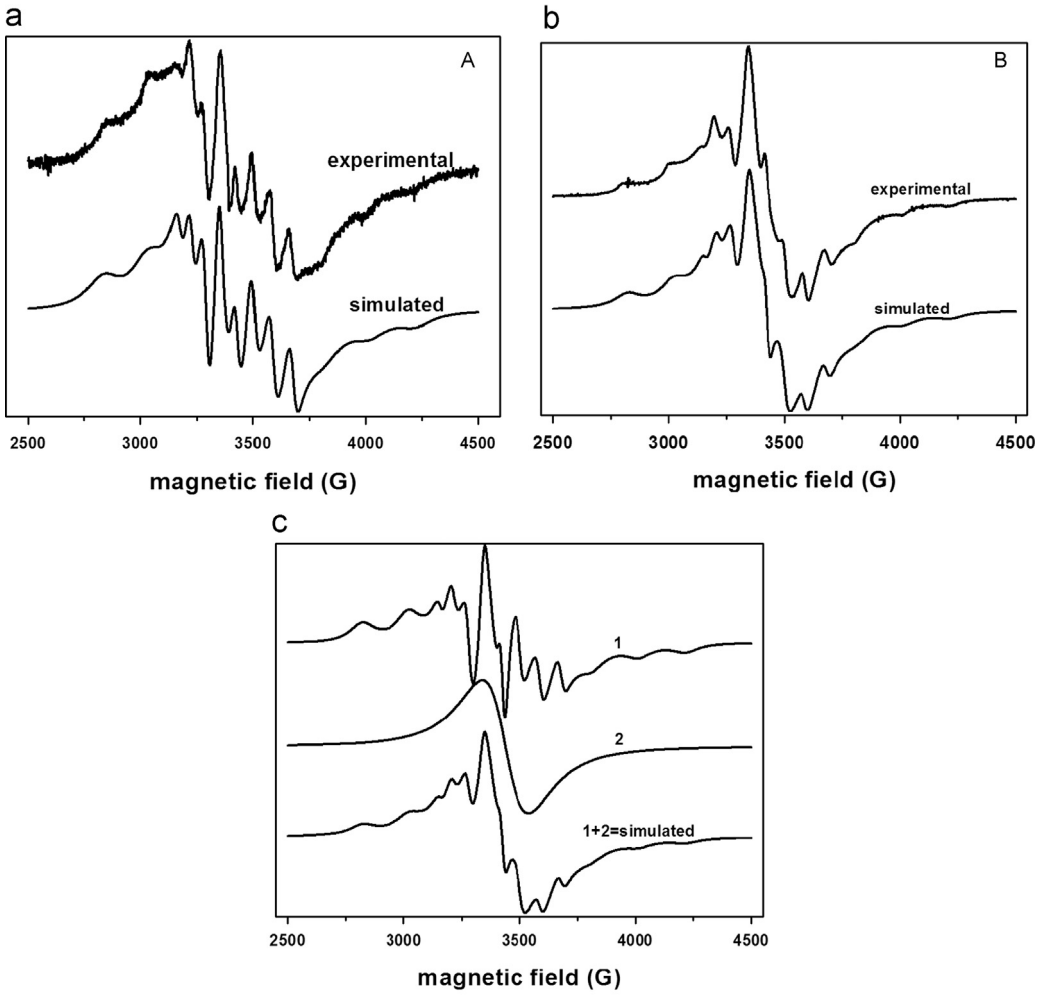

Fig. 9. EPR spectra of the $BiVO_4$ samples A and B. The graph (C) illustrates the contributions to the vanadium EPR spectrum from (1) anisotropic signal of isolated V^{4+} and (2) background signal of V^{4+} pairs or emanating from clustering of V^{4+} ions.

probabilities and the sample absorption may be then enhanced on a wide range of the visible spectrum. Thus, the electronic configurations of reduced vanadium influence the optical absorption and the charge transfer mechanism which may contribute to the photocatalytic activity of $BiVO_4$. On the other hand, a correlation between the conductivity and EPR measurements can be discussed to understand whether V^{4+} ions can act as charge carriers or charge traps on the conduction channels. In this aim, the concentration of V^{4+} ions was evaluated and compared between both samples (A, B). This concentration is determined from the integrated line intensity of the EPR signal and compared to a reference sample [23]. In the sample A, the concentration of $[V^{4+}]_A = 4.10^{16}$ spin/gram is one order of magnitude less than in the B sample ($[V^{4+}]_B = 4.10^{17}$ spin/gram). Thus, sample B favour a high concentration of reduced vanadium ions. In the same time, the conductivity is also higher. So, with respect to the V^{5+}–O^{2-} molecular bonds which account for the charge transfer within the crystalline structure, V^{4+} ions seem to favour the conductivity in such samples and may contribute also to the optical features.

4. Conclusions

$BiVO_4$ nanopowders were successfully synthesized by mechanochemical method and for the first time systematic investigations by dielectric and EPR spectroscopy were achieved. Depending on the synthesis parameters such as the milling time and BPR ratios, the structural and morphology features are modulated as well as the dielectric behaviour. Thus, the large quasi-static dielectric constant in nanostructured samples, twice higher than the value in bulk $BiVO_4$, indicates larger effects from interfacial polarisations involved at the grain boundaries and enhanced by large specific surfaces. The dielectric losses underline conduction phenomena for which the dc conductivities were estimated as well as their evolution with the temperature. Thermally activated conductivities were demonstrated with two main evolution regimes characterized by different activations energies and a crossover temperature around 310 K. A correlation was suggested between the dc conductivities, characteristic relaxation times and also with the structural and morphologies properties of the investigated samples. The paramagnetic and active electronic centres were investigated by EPR and assigned to V^{4+} ions involved in crystalline tetrahedral sites of $BiVO_4$ as clearly stated from the anisotropy of the EPR spectral parameters (*g*-tensors and hyperfine *A*-tensors). The electronic configuration inferred from EPR investigations was discussed as well as the role of V^{4+} in the conduction process of nanostructured $BiVO_4$ samples.

Acknowledgments

We acknowledge the financial support from European Union FP7 – NMP EU – Mexico program under grant agreement no. 263878/ by CONACYT no. 125141. Venkatesan Rajalingam is

also thankful for the scholarship jointly provided by SEP and CINVESTAV to pursue the doctoral study.

References

[1] A.K. Bhattacharya, K.K. Mallick, A. Hartridge, Mater. Lett. 30 (1997) 7.
[2] T.H. Yeom, Solid State Commun. 125 (10) (2003) 547.
[3] H.M. Zhang, J.B. Liu, H. Wang, W.X. Zhang, H. Yan, J. Nano Res. 10 (5) (2008) 768.
[4] N.C. Castillo, A. Heel, T. Graule, C. Pulgarin, Appl. Catal., B 95 (3-4) (2010) 335.
[5] W.I.F. David, I.G. Wood, J. Phys. C: Solid State Phys. 16 (1983) 5149.
[6] Y. Liang, T. Tsubota, L.P.A. Mooij, R. Van de Krol, J. Phys. Chem. C 115 (35) (2011) 17594.
[7] S. Charpentier, A. Kassiba, A. Bulou, M. Monthioux, M. Cauchetier, Eur. Phys. J. Appl. Phys. 8 (2) (1999) 111.
[8] S. Charpentier, A. Kassiba, J. Emery, M. Cauchetier, J. Phys. Condens. Matter 11 (1999) 4887.
[9] J.N. Torba, N.V. Golubko, E.A. Fortalnova, G.M. Kaleva, M.G. Safronenko, N.U. Venskovskii, E.D. Politova, Acta Phys. Pol. A 117 (2010) 24–26.
[10] K.V.R. Prasad, K.B.R. Varma, Mater. Chem. Phys. 38 (1998) 406–410.
[11] S.K. Pilli, T.E. Furtak, L.D. Brown, T.G. Deutsch, J.A. Turner, A.M. Herring, Energy Environ. Sci. 4 (2011) 5028.
[12] H. Jiang, H. Dai, X. Meng, L. Zhang, J. Deng, Y. Liu, C.T. Au, J. Environ. Sci. 24 (3) (2012) 449.
[13] A. Kassiba, M. Tabellout, S. Charpentier, N. Herlin, J.R. Emery, Solid Stat Commun. 115 (4) (2000) 389.
[14] M. Tabellout, A. Kassiba, A, S. Tkaczyk, S, L. Laskowski, J. Swiatek, J. Phys. Condens. Matter 18 (4) (2006) 1143.
[15] R. Venkatesan, S. Velumani, A. Kassiba, Mater. Chem. Phys. 135 (2012) 842–848.
[16] S. Havriliak, S. Negami, J. Polym. Symp. 14 (1966) 89.
[17] B. Li, B. Tang, S. Zhang, H. Jiang, J. Mater. Sci. 45 (23) (2010) 6461.
[18] A. Dutta, C. Bharti, T.P. Sinha, Mater. Res. Bull. 43 (2008) 1246.
[19] B. Hirschorn, M.E. Orazem, B. Tribollet, V. Vivier, I. Frateur, M. Musiani, J. Electrochem. Soc. 157 (12) (2010) C452.
[20] J. Macutkevic1, J. Banys1, A. Matulis Nonlin., Anal. Model. Control 9 (1) (2004) 75.
[21] A. Kassiba, R. Hrabanski, D. Bonhomme, A. Hader, J. Phys. Condens. Matter 7 (17) (1995) 3339.
[22] G. Oversluizen, R. Metselaar, J. Phys. C: Solid State Phys. 15 (1982) 4869.
[23] B. Pattier, M. Henderson, A. Poppl, A. Kassiba, A. Gibaud, J. Phys. Chem. B 114 (13) (2010) 4424.